A statistically selected *Chandra* sample of 20 galaxy clusters – II. Gas properties and cool core/non-cool core bimodality

Alastair J. R. Sanderson,[1]* Ewan O'Sullivan[2] and Trevor J. Ponman[1]

[1]*School of Physics and Astronomy, University of Birmingham, Edgbaston, Birmingham B15 2TT*
[2]*Harvard-Smithsonian Center for Astrophysics, 60 Garden Street, Cambridge, MA 02138, USA*

ABSTRACT

We investigate the thermodynamic and chemical structure of the intracluster medium (ICM) across a statistical sample of 20 galaxy clusters analysed with the *Chandra* X-ray satellite. In particular, we focus on the scaling properties of the gas density, metallicity and entropy and the comparison between clusters with and without cool cores (CCs). We find marked differences between the two categories except for the gas metallicity, which declines strongly with radius for all clusters ($Z \propto r^{-0.31}$), outside $\sim 0.02 r_{500}$. The scaling of gas entropy is non-self-similar and we find clear evidence of bimodality in the distribution of logarithmic slopes of the entropy profiles. With only one exception, the steeper sloped entropy profiles are found in CC clusters whereas the flatter slope population are all non-CC clusters. We explore the role of thermal conduction in stabilizing the ICM and conclude that this mechanism alone is sufficient to balance cooling in non-CC clusters. However, CC clusters appear to form a distinct population in which heating from feedback is required in addition to conduction. Under the assumption that non-CC clusters are thermally stabilized by conduction alone, we find the distribution of *Spitzer* conduction suppression factors, f_c, to be lognormal, with a log (base 10) mean of -1.50 ± 0.03 (i.e. $f_c = 0.032$) and log standard deviation 0.39 ± 0.02.

Key words: conduction – galaxies: clusters: general – cooling flows – X-rays: galaxies: clusters.

1 INTRODUCTION

The majority of baryons in collapsed massive haloes reside in a hot phase, in the form of a gaseous intracluster medium (ICM), with the remainder predominantly locked up in stars (Fukugita, Hogan & Peebles 1998; Gonzalez, Zaritsky & Zabludoff 2007). This hot gas serves as a reservoir of material to fuel not only star formation, but also black hole growth, as the ultimate endpoints of radiative cooling. Both these processes in turn give rise to feedback from subsequent supernova winds (Katz 1992; Strickland & Stevens 2000) and outbursts from active galactic nuclei (AGN; see McNamara & Nulsen 2007, for a recent review), respectively.

Given the considerable effectiveness of radiative cooling in depleting the hot gas, its dominance of the baryon budget in cluster haloes emphasizes the importance of feedback in order to restrict the excessive growth of galaxies (e.g. Cole 1991) and avoid a 'cooling crisis' (Balogh et al. 2001), which has long plagued cosmological simulations in which the effects of non-gravitational heating are neglected (e.g. Katz & White 1993; Suginohara & Ostriker 1998). The same feedback mechanism(s) may also be responsible for arresting

gas cooling in dense cluster cores (e.g. Peterson et al. 2001), where the development of a classical 'cooling flow' (Fabian 1994) appears to be truncated (Peterson & Fabian 2006).

A further indication of the importance of cooling is the discovery of short gas-cooling times in the inner regions of even non-cool core (CC) clusters (Sanderson, Ponman & O'Sullivan 2006, hereafter Paper I), as well as the quasi-universality of cooling-time profiles across a wide range of cluster masses (Voigt & Fabian 2004; Bauer et al. 2005; Paper I), despite the clear differences between the temperature profiles of CC and non-CC clusters (Paper I; e.g. Zhang et al. 2006; Pratt et al. 2007). The explanation for this dichotomy in the cluster population is the subject of current debate (e.g. Guo, Oh & Ruszkowski 2008; McCarthy et al. 2008), but is likely to involve galaxy feedback, given that cosmological simulations appear to overpredict the abundance of CCs in the cluster population (e.g. Kay et al. 2007) and that there is some question over the effectiveness of merging in permanently erasing CCs (Poole et al. 2006). However, the lack of evidence for *strong* shock heating from most AGN outbursts in cluster cores (McNamara & Nulsen 2007) presents a challenge to understanding how feedback alone is sufficient to offset cooling losses.

It is clear that a more complete picture of the thermodynamic state of hot gas in clusters is needed, in order both to solve the

*E-mail: ajrs@star.sr.bham.ac.uk

cooling-flow problem and tackle the broader issue of feedback between galaxies and the ICM. In pursuing these goals, it is necessary to map the thermodynamic state of the ICM across a wide mass range, including both CC and non-CC clusters, the latter of which are known to be under-represented in such detailed studies. This enables the gas entropy to be determined, which is a very sensitive probe of non-gravitational processes, as well as the metallicity, which acts as a tracer of supernova enrichment and gas mixing. We aim to do this using *Chandra* observations of nearby clusters, which is the only instrument able to reliably probe core gas properties on kpc scales, where the effects of baryon physics are greatest. The basis for this investigation is the statistical sample of Paper I comprising 20 galaxy clusters, in order to provide a representative survey of detailed cluster properties in the local Universe.

Throughout this paper, we adopt the following cosmological parameters: $H_0 = 70$ km s^{-1} Mpc^{-1}, $\Omega_m = 0.3$ and $\Omega_\Lambda = 0.7$. Throughout our spectral analysis, we have used XSPEC 11.3.2t, incorporating the solar abundance table of Grevesse & Sauval (1998), which is different from the default abundance table. Typically, this results in larger Fe abundances, by a factor of $\sim$1.4. All errors are 1σ, unless otherwise stated.

2 SAMPLE SELECTION

The objects studied in this paper comprise the statistical sample of 20 galaxy clusters observed with *Chandra* presented in Paper I. The sample contains the 20 highest flux clusters drawn from the 63 cluster, flux-limited sample of Ikebe et al. (2002), excluding those objects with extremely large angular sizes (the Coma, Fornax and Centaurus clusters), which are difficult to observe with *Chandra* owing to its limited field of view. The Ikebe et al. flux-limited sample was itself constructed from the HIFLUGS sample of Reiprich & Böhringer (2002), additionally selecting only those clusters lying above an absolute galactic latitude of 20 degrees and located outside of the Magellanic Clouds and the Virgo Cluster regions.

2.1 Re-analysis of *Chandra* data

Since the original analysis of the statistical sample data in Paper I, all but one of the *Chandra* observations have been reprocessed with uniform calibration by the *Chandra* X-ray Center (CXC) and we have re-analysed all the data accordingly. The only exception is Abell 2256 (ObsID 1386), which was observed at a frontend temperature of $-110°$ C: thus far, only data sets observed at $-120°$ C have been reprocessed, in order to provide a uniform calibration of most of the data in the *Chandra* archive.[1] Despite this, there is no indication that our results for Abell 2256 are anomalous in any way.

For the clusters Abell 401, Abell 496, Abell 1795, Abell 2142 and Abell 4038, longer observations are now available and, in the case of Abell 1795 & Abell 2142 these are with ACIS-I, giving the advantage of a wider field of view over the data sets analysed in Paper I. For Abell 478, however, we retain our original ACIS-S analysis (ObsID 1689) in favour of a newer ACIS-I observation, as the latter exposure is much shallower. Details of the new data sets analysed are given in Table 1 and key properties for the full sample are listed in Table 2. The data analysis and reduction were performed as detailed in Paper I, using version 3.4 of the standard

Table 1. Clusters from the statistical sample for which new observations have been analysed.

Name	Obsid[a]	Detector[b]	Data mode[c]
Abell 401	2309	I	F
Abell 496	4976	S	VF
Abell 1795	5289	I	VF
Abell 2142	5005	I	VF
Abell 4038	4992	I	VF

[a]*Chandra* observation identifier. [b]Denotes either ACIS-I or ACIS-S. [c]Telemetry data mode (either faint or very faint).

software, *Chandra* Interactive Analysis of Observations (CIAO[2]), incorporating CALDB version 3.4.2.

3 DATA ANALYSIS

Spectral fitting was performed as described in Paper I, using weighted response matrix files (RMFs) generated with the CIAO task 'MKACISRMF' for all cases, except Abell 2256 – the only non-reprocessed data set – where the older task 'MKRMF' was used instead. Spectra were fitted using an absorbed (WABS XSPEC component) APEC model over the energy range 0.5–7.0 keV for observations made with the ACIS-S detector, and 0.7–7.0 keV for those made with ACIS-I (as indicated in column 3 of Table 2). Spectra were grouped to a minimum of 20 counts per bin and fitted using the χ^2 statistic.

3.1 Cluster mean temperature and fiducial radius

Measurements of mean temperature, $\overline{T}$, and fiducial scaling radii are very important in scaling studies, in order to permit a fair comparison of properties across a wide range of cluster mass. In Paper I, we used an iterative scheme to determine both a core-excluded mean temperature and r_{500} (the radius enclosing a mean overdensity of 500 with respect to the critical density of the Universe), via the $M-T_X$ relation of Finoguenov, Reiprich & Böhringer (2001). However, we have subsequently refined this method in the following two ways, to improve the reliability of our results.

First, we have adopted the newer, *Chandra*-derived $M-T_X$ relation of Vikhlinin et al. (2006) which is based on clusters with high-quality observations, allowing direct measurements of gas properties at r_{500}. Secondly, we have now excluded a larger central region of the data ($0.15r_{500}$), to remove more completely any contaminating emission from strong central cooling that may occur in the core. Our chosen annular extraction region therefore spans the range 0.15–0.2r_{500}; we use 0.2r_{500} to exclude outer regions where data incompleteness begins to affect our sample, due to the restricted *Chandra* field of view. None the less, one advantage of using an outer annulus of 0.1–0.2r_{500} is that it provides a better measure of any central temperature drop (within 0.1r_{500}), as this range typically brackets the peak around the CC radius. Therefore, we retain the objective classifications of CC status determined in Paper I (and listed in Table 2), which were based on the significance of the temperature difference between the spectrum extracted in the range 0.1–0.2r_{500} compared to that measured inside 0.1r_{500}.

The temperatures in the $M-T_X$ relation of Vikhlinin et al. (2006) were based on an aperture extending out to r_{500}, excluding the

---

[1] For details, see http://cxc.harvard.edu/cda/repro3.html

[2] http://cxc.harvard.edu/ciao/

Table 2. Key properties of the sample, listed in order of increasing temperature.

Name	ObsID[a]	Detector[b]	Redshift	Mean kT^c (keV)	r_{500} (kpc)	Mean metallicity[c] (Solar)	CC status	$S^d_{0.1r_{500}}$ (keV cm^2)	Index[d]
NGC 5044	798	S	0.008	$1.17^{+0.04}_{-0.05}$	512^{+10}_{-10}	$0.37^{+0.09}_{-0.06}$	CC	50^{+27}_{-17}	$0.71^{+0.39}_{-0.09}$
Abell 262	2215	S	0.016	$2.08^{+0.11}_{-0.09}$	692^{+18}_{-15}	$0.38^{+0.10}_{-0.07}$	CC	126^{+48}_{-20}	$0.91^{+0.30}_{-0.13}$
Abell 1060	2220	I	0.012	$2.92^{+0.11}_{-0.11}$	829^{+16}_{-16}	$0.50^{+0.07}_{-0.07}$	non-CC	191^{+9}_{-7}	$0.44^{+0.03}_{-0.07}$
Abell 4038	4992	I	0.030	$3.04^{+0.07}_{-0.09}$	840^{+10}_{-13}	$0.60^{+0.07}_{-0.07}$	non-CC	136^{+8}_{-4}	$0.55^{+0.08}_{-0.14}$
Abell 1367	514	S	0.022	$3.22^{+0.18}_{-0.18}$	869^{+25}_{-26}	$0.34^{+0.10}_{-0.09}$	non-CC	275^{+10}_{-31}	$0.28^{+0.10}_{-0.09}$
Abell 2147	3211	I	0.035	$3.69^{+0.18}_{-0.18}$	928^{+23}_{-23}	$0.28^{+0.11}_{-0.10}$	non-CC	281^{+32}_{-59}	$0.43^{+0.27}_{-0.16}$
2A 0335+096	919	S	0.035	$4.09^{+0.13}_{-0.13}$	980^{+16}_{-16}	$0.79^{+0.11}_{-0.11}$	CC	99^{+20}_{-20}	$1.12^{+0.22}_{-0.16}$
Abell 2199	497	S	0.030	$4.50^{+0.20}_{-0.24}$	1033^{+23}_{-29}	$0.79^{+0.14}_{-0.14}$	CC	165^{+17}_{-33}	$0.76^{+0.09}_{-0.06}$
Abell 496	4976	S	0.033	$4.80^{+0.15}_{-0.14}$	1067^{+16}_{-16}	$0.66^{+0.09}_{-0.08}$	CC	162^{+55}_{-34}	$0.93^{+0.32}_{-0.07}$
Abell 1795	5289	I	0.062	$5.62^{+0.36}_{-0.35}$	1144^{+37}_{-38}	$0.26^{+0.10}_{-0.10}$	CC	189^{+21}_{-35}	$0.99^{+0.33}_{-0.08}$
Abell 3571	4203	S	0.039	$6.41^{+0.23}_{-0.23}$	1239^{+23}_{-23}	$0.75^{+0.11}_{-0.11}$	non-CC	279^{+9}_{-7}	$0.44^{+0.04}_{-0.04}$
Abell 2256	1386	I	0.058	$6.52^{+0.39}_{-0.36}$	1239^{+38}_{-36}	$0.98^{+0.22}_{-0.21}$	non-CC	344^{+24}_{-158}	$0.47^{+0.47}_{-0.16}$
Abell 85	904	I	0.059	$6.64^{+0.20}_{-0.20}$	1251^{+19}_{-19}	$0.56^{+0.07}_{-0.07}$	CC	193^{+16}_{-20}	$0.90^{+0.14}_{-0.09}$
Abell 3558	1646	S	0.048	$7.17^{+0.49}_{-0.46}$	1309^{+46}_{-44}	$1.00^{+0.21}_{-0.20}$	non-CC	304^{+28}_{-53}	$0.62^{+0.30}_{-0.11}$
Abell 3667	889	I	0.056	$7.60^{+0.38}_{-0.37}$	1345^{+34}_{-35}	$0.51^{+0.10}_{-0.10}$	non-CC	407^{+46}_{-67}	$0.57^{+0.17}_{-0.09}$
Abell 478	1669	S	0.088	$8.23^{+0.26}_{-0.26}$	1381^{+23}_{-23}	$0.50^{+0.07}_{-0.07}$	CC	190^{+18}_{-8}	$1.03^{+0.21}_{-0.06}$
Abell 3266	899	I	0.055	$8.38^{+0.67}_{-0.43}$	1417^{+58}_{-38}	$0.39^{+0.11}_{-0.11}$	non-CC	528^{+19}_{-36}	$0.48^{+0.09}_{-0.09}$
Abell 2029	4977	S	0.077	$8.96^{+0.30}_{-0.30}$	1452^{+25}_{-25}	$0.60^{+0.07}_{-0.07}$	CC	257^{+20}_{-49}	$0.90^{+0.21}_{-0.08}$
Abell 401	2309	I	0.074	$9.16^{+1.41}_{-1.06}$	1471^{+114}_{-92}	$0.26^{+0.22}_{-0.23}$	non-CC	427^{+55}_{-56}	$0.45^{+0.15}_{-0.11}$
Abell 2142	5005	I	0.091	$9.50^{+0.43}_{-0.42}$	1487^{+34}_{-35}	$0.44^{+0.07}_{-0.07}$	non-CC	295^{+19}_{-18}	$0.94^{+0.06}_{-0.17}$

[a]*Chandra* observation identifier. [b]ACIS detector. [c]Measured between 0.15 and $0.2r_{500}$ (see Section 3.1). [d]Parameters of the power-law fit to the entropy profile (see Section 4.2.1). Errors are 1σ.

central 70 kpc. Since cluster temperature profiles generally decline monotonically with radius outside of any CC (e.g. Vikhlinin et al. 2005; Pratt et al. 2007), it is therefore necessary to allow for a bias factor that would shift temperature measurements within $0.2r_{500}$ higher compared to those made within r_{500}. This was done by comparing the temperatures obtained using the iterative method of Paper I in the range 0.15–$0.2r_{500}$ for seven clusters from the sample of Vikhlinin et al. (2006) which were analysed in this work and in a companion analysis of galaxy groups (O'Sullivan et al., in preparation), namely Abell 262, 478, 1795, 2029 and MKW 4, MS1157 and USGCS152. The aim of this process was to determine a multiplicative factor to apply uniformly to the temperatures measured in the range 0.15–$0.2r_{500}$ to bring them into line with those measured in the Vikhlinin et al. aperture. The determination of this rescale factor was also iterative, and the procedure was as follows.

First, a mean temperature ($\overline{T}$) was measured iteratively in the range 0.15–$0.2r_{500}$ using the Vikhlinin et al. M–T_X relation to achieve convergence for each of the six clusters common to both samples. Then, a rescale factor was calculated as the mean ratio of these temperatures to the corresponding ones quoted in Vikhlinin et al. (2006). Secondly, the determination of $\overline{T}$ in the range 0.15–$0.2r_{500}$ was repeated, using this rescale factor to adjust the measured temperature before using equation (1) to calculate r_{500}. The process was repeated until convergence of the rescale factor, f, whose final value was determined to be 0.96, i.e. temperatures measured in our aperture were 4 per cent hotter than those measured by Vikhlinin et al. For a cluster of redshift, z, the radius is given by

$$r_{500} = \frac{f \times 484.7 \times \overline{T}^{-0.527}}{E(z)} \text{ kpc,} \tag{1}$$

where $f = 0.96$ is a rescale factor to convert temperatures measured in the range 0.15–$0.2r_{500}$ with those in the range 70 kpc–r_{500} and

$$E(z) = (1+z)\sqrt{1 + (z\,\Omega_m) + \frac{\Omega_\Lambda}{(1+z)^2} - \Omega_\Lambda}\,. \tag{2}$$

A comparison between these new temperatures and those from the original Ikebe et al. (2002) parent sample is shown plotted in Fig. 1. There is slightly better agreement between our new temperatures and those of Ikebe et al. amongst the hottest clusters than was obtained using the measurements from Paper I, although the difference between this plot and fig. 2 from Paper I is fairly small.[3] The Ikebe et al. (2002) mean temperatures were based on a two-component spectral fit to the full cluster emission, which would likely result in lower $\overline{T}$ values for the hottest clusters, as pointed out in Paper I. An additional factor is a possible bias in temperature estimates for hotter clusters ($\gtrsim$4–5 keV) resulting from errors in the *Chandra* response matrix (as described in Sun et al. 2008, and references therein), which could lead to overestimates of $\overline{T}$. Our final $\overline{T}$ values are listed in Table 2, together with the mean metallicity measured in the same aperture (see Section 4.3).

Although the M–T_X relation of Vikhlinin et al. (2006) comprises clusters hotter than $\sim$2.3 keV, we none the less have verified that the masses of our cooler galaxy groups (O'Sullivan et al., in preparation) are consistent with it. Furthermore, we note that the recent *Chandra* study of 40 galaxy groups by Sun et al. (2008) finds only weak

[3] Note. The CC status of the points in fig. 2 of Paper I was incorrectly labelled.
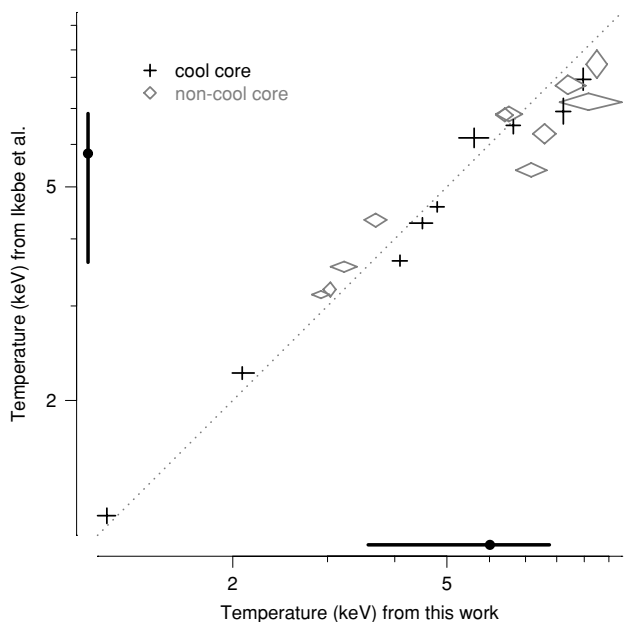
Figure 1. A comparison of the new mean temperatures from this work ($0.15-0.2r_{500}$) and those of Ikebe et al. (2002), showing the line of equality. The dots and solid lines indicate the marginal medians and interquartile ranges.

evidence (at the 1.5σ level) for a steepening of the $M-T_X$ relation in groups compared to clusters. This therefore justifies our inclusion of a mixture of clusters and groups in the seven systems used to calibrate our modification of the Vikhlinin et al. $M-T_X$ relation for temperatures measured in the aperture $0.15-0.2r_{500}$.

3.2 Spectral profiles and deprojection analysis

The results which follow are based on the deprojection analysis method described in Paper I, to derive three-dimensional gas temperature and density profiles. To stabilize the fitting, the Galactic absorbing column and gas metallicity were fixed at values obtained by fitting each annulus separately prior to the deprojection. Consequently, the gas metallicity results presented in Section 4.3 are projected quantities. For some clusters, it was necessary to freeze the absorbing column at the galactic H I value, since unfeasibly low values were otherwise obtained in many of the annular bins: full details can be found in Paper I. Similarly, in a number of cases the deprojected temperature had to be fixed at its projected value, to produce a stable fit, exactly as was done in Paper I.

4 RESULTS

4.1 Gas density

Fig. 2 shows the gas density as a function of scaled radius for the sample, colour-coded by mean temperature and split according to CC status. Following Paper I, in order to clarify the underlying trend in each profile, the raw data points have been fitted with a locally weighted regression in log–log space, using the task 'LOESS' in version 2.7 of the R statistical software environment package[4] (R Development Core Team 2008). It is immediately apparent from

[4] http://www.r-project.org
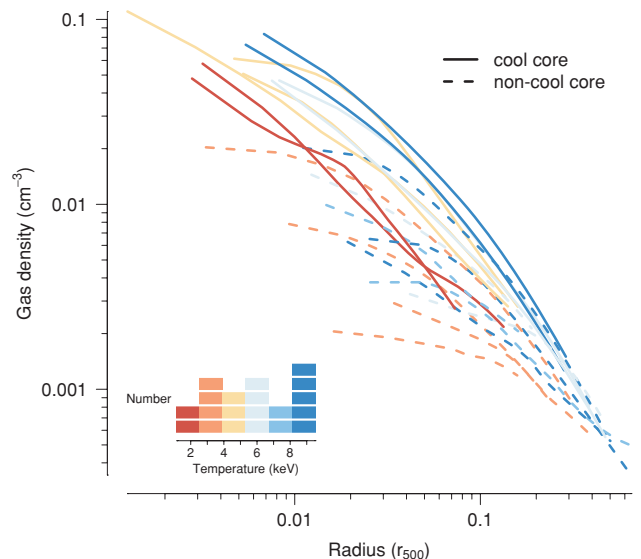
Figure 2. Gas density profiles for each cluster, scaled to r_{500} and coloured according to the mean cluster temperature, depicted by the inset histogram. Each curve represents a locally weighted fit to the data points, to suppress small-scale fluctuations (see the text for details).

Fig. 2 that the profiles do not scale self-similarly, which would imply constant density at a given fraction of r_{500}. There is a wide dispersion in the core, with a factor of ~ 30 range in ρ_{gas} at $0.01r_{500}$, dropping to a factor of ~ 5 spread at $0.1r_{500}$. At larger radius (beyond the peak in the temperature profile at $\sim 0.15r_{500}$; Paper I), there is a clear convergence in the profiles, despite the diminishing data coverage due to the limits of the *Chandra* field of view.

It is clear from Fig. 2 that the CC clusters have systematically denser and more cuspy cores, consistent with the decline in gas temperature (scaling with $r^{\sim 0.4}$; Paper I) that must be counteracted by a rising density in order to maintain pressure equilibrium. The near power-law shape of the density profiles in the CC clusters is also consistent with a cooling-dominated regime, as indicated by the simulations of Ettori & Brighenti (2008), who find $\rho_{gas} \propto r^{-1.2}$ for evolved CC clusters (after 10 Gyr). Within each CC category, there is also a systematic trend towards lower ICM densities in cooler systems. This may reflect gas depletion due to cooling out of the hot phase, or could be caused by non-gravitational heating expelling material out of the core. These findings are consistent with the recent study of Croston et al. (2008), based on a representative sample of 31 clusters analysed with *XMM–Newton*.

4.2 Gas entropy

The entropy of the gas is a key parameter, which provides a measure of the thermodynamic state of the ICM and is conserved in any adiabatic process (see e.g. Bower 1997; Tozzi & Norman 2001; Voit et al. 2002). We define entropy as $S = kT/\rho_{gas}^{2/3}$ (e.g. Ponman, Cannon & Navarro 1999), which implies $S \propto kT$ for self-similar clusters. Within a virialized halo, the gas entropy is initially set by shock heating, which leads to a radial variation of the form $S \propto r^{1.1}$ for a simple spherical collapse (Tozzi & Norman 2001). Despite radiative cooling in the cores of clusters lowering the entropy, its power-law variation with radius is nevertheless largely preserved, with approximately the same logarithmic slope as in the outskirts (e.g. Ettori & Brighenti 2008), leading to the expectation of a near-proportionality between entropy and physical (i.e. unscaled) radius,
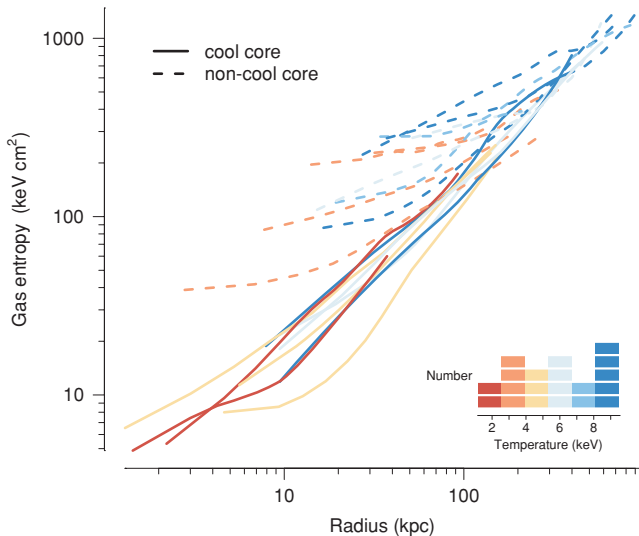
Figure 3. Gas entropy profiles as a function of physical radius, colour-coded by cluster mean temperature. Each curve represents a locally weighted fit to the data points, to suppress small-scale fluctuations (see the text for details).

Figure 4. Residuals from the power-law fits to the entropy profiles, normalized by the predicted value and plotted against scaled radius for each cluster. A single value is omitted (0.76 at $0.0047r_{500}$, for the innermost point of 2A 0335+096) to optimize the y-axis scale range for viewing the data.

regardless of halo mass. This can be seen in Fig. 3 which shows gas entropy profiles as a function of radius in kpc for the sample, separated by CC status and colour-coded by mean temperature.

The distinction between CC and non-CC clusters is very clear from Fig. 3, with the latter having significantly higher entropy in the core and the divergence between the two types occurring within $\sim$40 kpc, at an entropy level of $\sim$80 keV cm^2. The CC entropy profiles are tightly grouped and show no obvious sign of the transition between the shock-heating regime in the outskirts and the cooling-dominated core. In contrast, the non-CC profiles show a much larger scatter in normalization, which may reflect the diversity of heating processes affecting them. Alternatively, it could be that cooling acts to regulate the entropy of CC clusters so as to suppress the scatter between them, which may also account for the apparent universality seen in the cooling-time profiles of the sample (Paper I).

4.2.1 Entropy profile fitting

In order to characterize the form of the entropy profiles plotted in Fig. 3, we fitted power laws to each cluster profile to quantify the logarithmic slope of the relationship. However, it can be seen from Fig. 3 that at small radii the profiles tend to flatten and therefore deviate from a simple power-law form (see also Donahue et al. 2006, for example). Nevertheless, a power law provides a simple and reasonably effective description of the majority of the profile in all cases which enables the 'flatness' of the curves to be characterized. We have additionally employed a quantile regression technique to perform the fitting, in order to provide resistance to any such outliers. This form of regression minimizes the sum of absolute residuals, rather than the sum of squared residuals, and thus is analogous to determining the median as an estimator of the mean (Koenker 2005). The algorithm used is the 'RQ' function from the QUANTREG package in R[5] and was executed as an unweighted linear fit in log–log space. Table 2 lists the best-fitting normalization (at $0.1r_{500}$) and power-law index (i.e. logarithmic slope) for each cluster, together with the corresponding 1σ errors.

[5] See the tutorial at http://www.astrostatistics.psu.edu/su07/R/reg.html
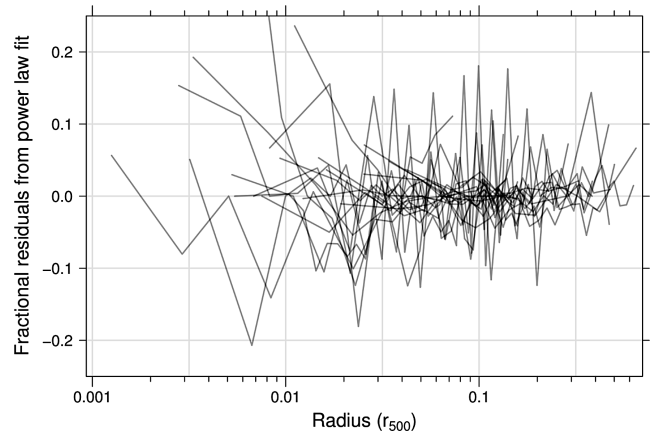
To assess the suitability of a power law for describing the entropy profiles, we show in Fig. 4 the residuals from the best-fitting model as a function of scaled radius, for each cluster. We have normalized the residuals by the predicted model values rather than the measurement errors on the entropy, since the fit was performed using unweighted quantile regression rather than by minimizing χ^2. This approach allows for the fact that real clusters exhibit intrinsic deviations from simple radial models in excess of the statistical scatter associated with measurement errors. It can be seen that in general the power-law fits do a reasonable job of describing the data, with the majority of residuals contained within $\sim$5 per cent of the best fit. However, while there is no obvious sign of any strong systematic trends with radius, there is some indication of an excess entropy above the model at very small radii ($\lesssim 0.03r_{500}$) for a few of the clusters, consistent with the flattening in the entropy profiles of nine CC clusters found by Donahue et al. (2006). Nevertheless, we restrict our use of the power-law fits to the entropy profile to a larger radius ($0.1r_{500}$), which is not affected by any such systematic departure from a power-law form.

There is no evidence of any systematic variation in the logarithmic slope of the entropy profile with mean temperature across the sample, as plotted in Fig. 5. However, CC and non-CC clusters are clearly segregated in the plot, occupying higher and lower values of the entropy index, respectively. The only exception is Abell 2142 – the archetypal 'cold front' cluster (Markevitch et al. 2000) – which was classified as a non-CC cluster in Paper I, as its CC ratio was found to be only marginally significant ($\sim$2σ; Paper I). Notwithstanding the CC status of the clusters, it is reasonable to ask if there is any evidence for bimodality in the distribution of logarithmic slope values in Fig. 5, and we address this specific issue in Section 5.

4.2.2 Entropy scaling

The effectiveness of entropy as a probe of non-gravitational physics in the ICM is best exploited by studying its variation with mean temperature, which is expected to be linear in the case of simple self-similarity. However, the strong dependence of entropy on radius raises the issue of at what point to measure entropy in order to consider its variation from cluster to cluster. The issue is further complicated by the fact that the gas entropy within a cluster
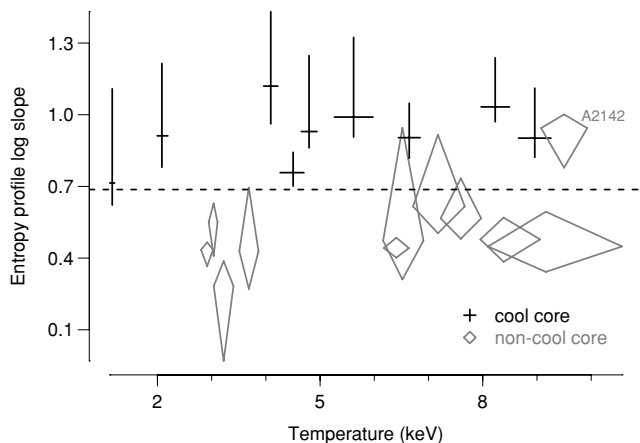
Figure 5. Best-fitting logarithmic slope of the entropy profile as a function of mean system temperature. The dashed line marks the crossover point between the two Gaussian distributions of values from Section 5 and the outlier Abell 2142 is labelled (see text for details).

bridges two distinct regimes: the cooling-dominated core and the outskirts, where the effects of shock heating from infall prevail. The first measurements of entropy scaling were made at a fiducial radius of $0.1r_{200}$ (Ponman, Cannon & Navarro 1999; Lloyd-Davies, Ponman & Canon 2000) in order to sample the region between these two regimes. However, Pratt, Arnaud & Pointecouteau (2006) find consistent results for the scaling with temperature of entropy when measured a range of radii at fractions of r_{200} of 0.1, 0.2, 0.3 and 0.5 in the range $b = 0.5$–0.6 for $S \propto \overline{T}^b$.

Taking the power-law fits to the entropy profiles performed above, we plot in Fig. 6 entropy versus $\overline{T}$ for the sample using the normalization value, corresponding to a fiducial radius of $0.1r_{500}$. Also shown are power-law fits to the CC and non-CC clusters separately, performed in log–log space using the bivariate correlated errors and intrinsic scatter (BCES)-weighted orthogonal regression method of Akritas & Bershady (1996). The logarithmic slopes of these lines
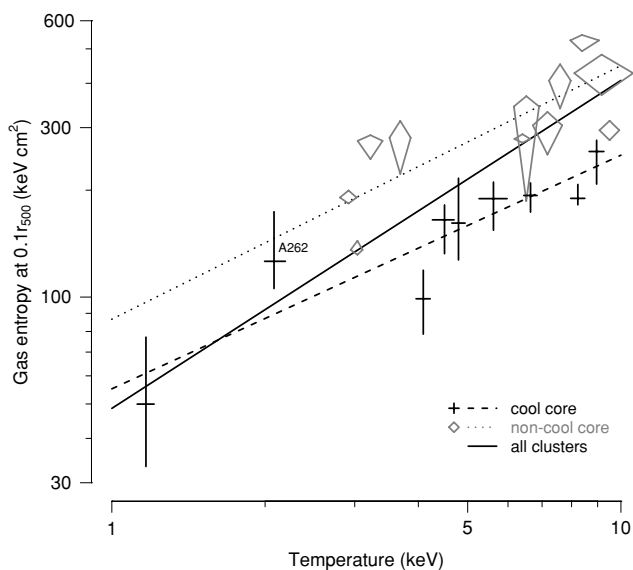
correspond to an entropy scaling of the form $S \propto \overline{T}^b$ with $b = 0.66 \pm 0.10$ and 0.71 ± 0.21 for the CC and non-CC clusters, respectively. These results are in good agreement with the value of 0.65 ± 0.05 similarly determined by Ponman, Sanderson & Finoguenov (2003), at a fiducial radius of $0.1r_{200}$, as well as with the values found by Pratt et al. (2006) at a series of radii and using a number of regression methods.

The CC and non-CC points are generally well separated with respect to their corresponding best-fitting power laws in Fig. 6. However, in the case of the CC cluster Abell 262, the (albeit large) error bar overlaps significantly with the *non*-CC best-fitting line. While this poor cluster does have a strong negative central temperature gradient, it is also known to possess a number of cavity and ripple features coincident with low-frequency radio emission (Blanton et al. 2004). It is therefore possible that AGN activity in the core might have boosted the entropy at $0.1r_{500}$ to shift this cluster towards the non-CC regression line. Nevertheless, a number of the other CC clusters also host ghost cavities (see table 2 in Paper I), which evidently have not significantly biased their location in Fig. 6.

While the separate fits to the CC and non-CC clusters in Fig. 6 yield results consistent with a *non*-self-similar entropy scaling, the two sets of points are clearly offset from each other. It is interesting to note that a BCES orthogonal regression fit to all the 20 clusters combined yields a much steeper logarithmic slope of 0.92 ± 0.12, which *is* consistent with self-similar scaling. To check this result, we repeated the individual power-law fits using a pivot point of $0.15r_{500}$ and performed the same regression of the normalization versus mean temperature to obtain the following logarithmic slopes:

1.06 ± 0.16 (all clusters combined),
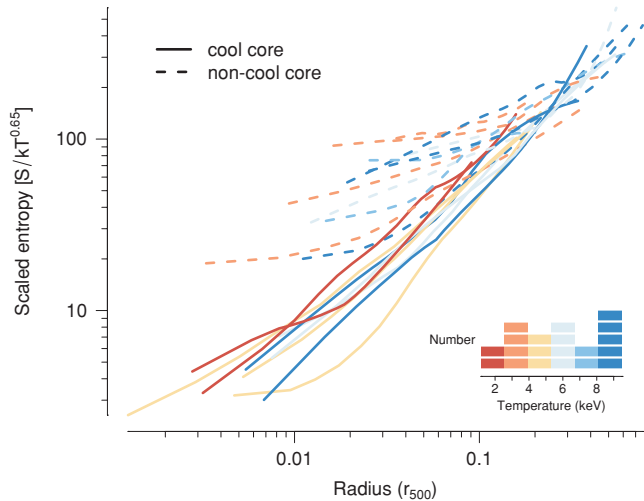0.65 ± 0.10 (CC),
0.65 ± 0.26 (non-CC).

Thus, it is possible that similarity breaking can occur in the separate CC/non-CC cluster subpopulations in such a way as to produce fully self-similar scaling in an analysis which combines the two types. On the other hand, if we exclude the coolest system (NGC 5044) from the fit, the resulting best-fitting slope for the whole sample (0.89 ± 0.22) is consistent at the 1σ level with the values obtained for the separate CC and non-CC subsamples.

Given the broad agreement in the dependence on temperature of the entropy scaling, we show in Fig. 7 entropy profiles as a function of r/r_{500} normalized by the factor $T^{0.65}$ from Ponman et al. (2003). It can be seen that this empirical scaling brings the curves into fairly close alignment. There is, however, some indication of a systematic dispersion in the profiles, indicating that gas entropy may vary less strongly with cluster mean temperature than $T^{0.65}$, as also suggested by the results of Pratt et al. (2006) when measuring entropy at $0.1r_{200}$. In order to explore the entropy scaling across a range of radii, rather than at particular spot value, we modelled the variation of entropy in terms of both scaled radius *and* mean temperature using the following expression:

$$S = S' \left(\frac{r}{0.1r_{500}} \right)^a \left(\frac{\overline{T}}{5\,\text{keV}} \right)^b. \tag{3}$$

This parametrization has the advantage of allowing the scaling of entropy with both radius and temperature to be determined simultaneously. The results of performing an unweighted quantile regression fit in log–log space of equation (3) to the entire sample are summarized in Table 3. Only data in the range $0.02 < r/r_{500} < 0.2$ were included to ensure completeness in the radial coverage.

The resulting values of a agree well with the results from the individual power-law fits to each cluster described previously in

Figure 6. Entropy at $0.1r_{500}$ as a function of mean temperature, from a power-law fit to the entropy profile of each cluster. The lines are the best-fitting power law, with logarithmic slopes of 0.66 ± 0.10, 0.71 ± 0.21 and 0.92 ± 0.12 for the CC, non-CC and combined clusters, respectively.

Figure 7. Entropy profiles, scaled with the Ponman et al. (2003) empirical factor of $\overline{T}^{-0.65}$ versus scaled radius, colour-coded by cluster mean temperature. Each curve represents a locally weighted fit to the data points, to suppress small-scale fluctuations (see the text for details).

Table 3. Results from fitting equation (3) to the entire sample, as well as separately to the combined CC and non-CC clusters. Errors are 1σ; see text for details.

Sample	S' (keV cm^2)	a	b
All	214^{+10}_{-11}	$0.95^{+0.10}_{-0.08}$	$0.56^{+0.11}_{-0.08}$
CC	161^{+7}_{-10}	$1.05^{+0.07}_{-0.15}$	$0.49^{+0.07}_{-0.13}$
NCC	259^{+6}_{-4}	$0.51^{+0.09}_{-0.06}$	$0.52^{+0.08}_{-0.07}$

Section 4.2.1. It can also be seen that the fit to the entire sample yields a dependency on mean temperature such that $S \propto \overline{T}^b$, with $b = 0.56^{+0.11}_{-0.08}$ slightly lower but still in agreement with the scaling of $\overline{T}^{0.65\pm0.05}$ found by Ponman et al. (2003), which was evaluated at a radius of $0.1\,r_{200}$ – roughly $0.15\,r_{500}$ (Sanderson & Ponman 2003). A fit to the combined CC and non-CC clusters separately yields values of $b = 0.49^{+0.07}_{-0.13}$ and $b = 0.52^{+0.08}_{-0.07}$, respectively, demonstrating that this weaker dependence of entropy on system temperature persists. This result is strongly inconsistent with a self-similar scaling of $S \propto \overline{T}$ (i.e. $b = 1$) demonstrating the impact of non-gravitational physics in influencing the hot gas (see Ponman et al. 2003, for example, for further discussion), but extends beyond the finding of Ponman et al. in that it applies across a range of radii spanning an order of magnitude, as opposed to being determined at only a fixed spot value. Furthermore, the fact that this result is essentially unchanged when fitting the CC and non-CC clusters separately (see Table 3) demonstrates the universality of this modified entropy scaling, at least in the range $0.02 < r/r_{500} < 0.2$.

However, the difference between CC and non-CC clusters is very clear when considering the variation of entropy with radius, $S \propto r^a$. Here, the corresponding logarithmic slopes are $a = 1.05^{+0.07}_{-0.15}$ and $0.51^{+0.09}_{-0.06}$, respectively, compared to $0.95^{+0.10}_{-0.08}$ for the entire sample. The flatness of the best-fitting non-CC entropy profile compared to that for the CC clusters is further underscored by the difference in normalization at the fiducial 'pivot point' in equation (3) (at $0.1\,r_{500}$ for $\overline{T} = 5$ keV), yielding values of $S' = 259^{+6}_{-4}$ keV cm^2 compared to 161^{+7}_{-10} keV cm^2, respectively. The results from the combined
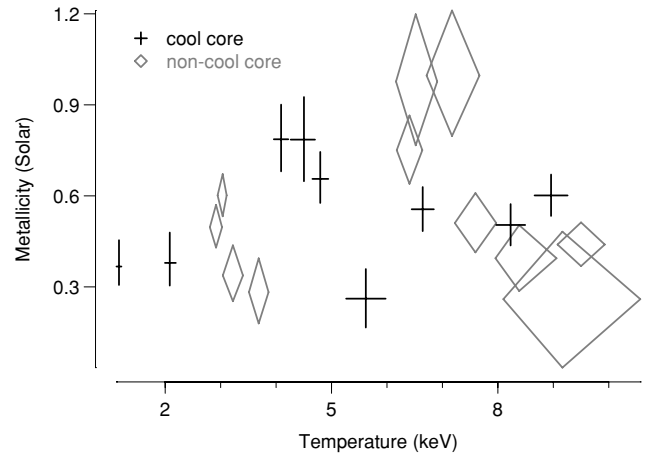
Figure 8. Gas metallicity (Grevesse & Sauval 1998 abundances) versus mean temperature, both measured in the range $0.15 \leq r/r_{500} \leq 0.2$.

fit of equation (3) are in good agreement with the results from the power-law fits to the individual cluster entropy profiles. They are also consistent with the logarithmic slope of 0.95 ± 0.02 (Piffaretti et al. 2005) and 1.08 ± 0.04 (Pratt et al. 2006) from two separate *XMM–Newton* analyses of CC clusters, as well as the values of slopes in the range 1–1.3 from the *Chandra* analysis of nine CC clusters by Donahue et al. (2006).

4.3 Metallicity of the ICM

The metallicity of the ICM is an important tracer of galaxy feedback via supernova-driven winds, which eject both metals and energy into the hot gas (e.g. Strickland & Stevens 2000). Fig. 8 shows the mean metallicity against mean temperature for the sample (see Table 2), both evaluated in the range $0.15 \leq r/r_{500} \leq 0.2$, identified according to CC status. There is no indication of any trend in the data or of any systematic difference between CC and non-CC clusters; the mean value across the entire sample is 0.55 Solar, with a standard deviation of 0.22.

To explore radial trends, we use the metallicity values determined in the projected annular spectral fitting, which were taken as fixed inputs in the deprojection analysis as described in Section 3.2 and Paper I. The fact that these values are not deprojected will tend to smooth out gradients slightly. However, Rasmussen & Ponman (2007) demonstrate that this is a small effect and that deprojected metallicity data typically suffer from large instabilities which add significantly to the noise, particularly given the poorer constraints on this parameter compared to temperature or density.

Fig. 9 shows the individual projected metallicity profiles as a function of scaled radius for the sample, split by CC status and colour-coded by mean temperature. The curves represent a locally weighted fit to the data, using the LOESS function described in Section 4.1 and it can clearly be seen that the metallicity declines with radius beyond ~ 0.01–$0.02\,r_{500}$ in almost every case, for both CC and non-CC clusters. Within this radius, the dispersion in metallicity increases noticeably; some clusters show a strongly peaked metallicity profile (in particular Abell 85 and Abell 2029), whereas others have metal-deficient central cores. More specifically, the three most peaked profiles are all hot clusters, whereas the coolest clusters show sharp central declines. It is not clear what is responsible for this strong divergence in behaviour, but it occurs on a scale of roughly $0.02\,r_{500}$ ($\sim$20–30 kpc), which is comparable to the size of the central galaxy. This also coincides with the region where the gas
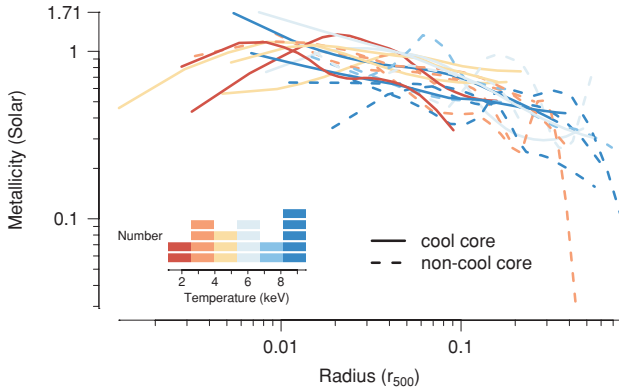
Figure 9. Projected gas metallicity profiles (using Grevesse & Sauval 1998 abundances) for each cluster, scaled to r_{500} and coloured according to the mean cluster temperature, depicted by the inset histogram. Each curve represents a locally weighted fit to the data points, to suppress small-scale fluctuations (see the text for details).

density and entropy profiles also become widely dispersed (Figs 2 and 7).

Regardless of any difference between CC and non-CC clusters at small radii, it is clear that the point where the metallicity begins to decline strongly towards the cluster outskirts lies well within the typical cooling radius of $\sim 0.15 r_{500}$ (Paper I). The fact that the metallicity profiles of all the clusters are quite similar beyond this point suggests that the enrichment of the ICM is insensitive to those factors responsible for determining CC status. The finding that metallicity declines strongly with radius in all the clusters is apparently at odds with the study of De Grandi & Molendi (2001), who concluded that the abundance profiles for the eight non-CC clusters in their *BeppoSAX* sample were consistent with being constant. However, examination of fig. 2 from De Grandi & Molendi (2001) shows that, with the exception of only a few outliers, there is an indication of a general decline in metallicity with increasing radius in their non-CC clusters. Furthermore, we note that Baldi et al. (2007) also found no difference between CC and non-CC gas metallicity profiles, outside $\sim 0.1 r_{180}$ in their analysis of 12 hot clusters observed with *Chandra*.

To highlight the trend in metallicity with radius, we show the mean CC and non-CC profiles in Fig. 10, grouped to a total of five bins in each case, with error bars indicating the standard deviation within each bin. Apart from a slightly larger dispersion in the non-CC bins, there is very little difference between the two profiles and no indication in either case of any flattening off at large radii. Interestingly, the *BeppoSAX* average CC profile of De Grandi et al. (2004) shows a sharp levelling off in metallicity at around 0.4 Solar (abundances Grevesse & Sauval 1998) at $0.2 r_{200}$, which corresponds to roughly $0.3 r_{500}$ – close to the limit of our *Chandra* data but otherwise consistent with the outer bin of Fig. 10, so we cannot rule out a flattening beyond this point.

However, in contrast, the De Grandi et al. (2004) non-CC profile is both flatter and lower in normalization (albeit only at $\sim 2\sigma$) and thus rather different from our own. Of their 10 non-CC clusters, only three are present in our sample (A1367, A2256 and A3266; they classify A2142 and A3571 as CC clusters) and their profiles for these systems appear to be reasonably consistent with our own within the region covered by *Chandra*. The differences between CC and non-CC clusters seen by De Grandi et al. (2004) appear to originate in the somewhat low and fairly flat abundance profiles of several non-CC clusters in their sample, whereas the non-CC
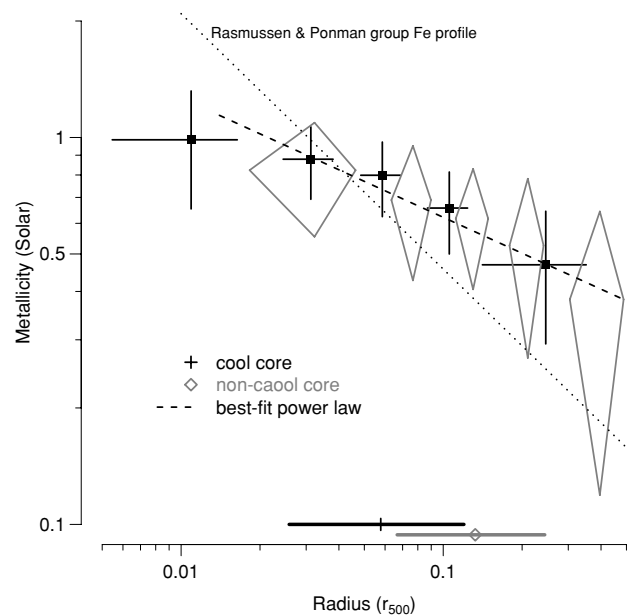
Figure 10. Average gas metallicity profiles for CC and non-CC clusters. Each bin represents the mean of a roughly equal number of points and the error bars show the standard deviation in both directions. The dashed line is the best-fitting power law to the unbinned data beyond $0.014 r/r_{500}$ and the dotted line is a fit to the iron abundances in 15 galaxy groups from Rasmussen & Ponman (2007, see text for details). The points and horizontal lines indicate the medians and interquartile ranges of the CC and non-CC raw data points.

clusters in our sample do not appear to include such cases. Notwithstanding this difference in samples, we note that Baldi et al. (2007) measure a similar radial decline to us, with essentially no difference between CC and non-CC clusters, albeit with the exception of their central bin. As mentioned above, cluster metallicity profiles appear to exhibit greater dispersion on the scale of the central galaxy, so some difference from sample to sample is to be expected in this region.

The data in Fig. 10 appear to be reasonably consistent with a power law, so we have fitted such a function in log–log space, using the quantile regression method outlined in Section 4.2.1. In order to exclude the core region where the profile flattens and the profile diverge substantially ($r \sim 0.014 r_{500}$; Fig. 9), we performed separate fits inside and outside this radius, combining both the CC and non-CC data. The results for the inner region ($r < 0.014 r_{500}$) are

$$\log_{10}(Z/Z_\odot) = 0.39^{+0.03}_{-0.22} \log_{10}(r/r_{500}) + 0.82^{+0.06}_{-0.4},$$

while those for the outer region ($r \geq 0.014 r_{500}$) are

$$\log_{10}(Z/Z_\odot) = -0.31^{+0.03}_{-0.05} \log_{10}(r/r_{500}) - 0.51^{+0.03}_{-0.07}.$$

By comparison, the metallicity profiles of galaxy groups appear to be somewhat steeper in their decline at large radii. The recent analysis of 15 groups with *Chandra* data by Rasmussen & Ponman (2007) – also using Grevesse & Sauval (1998) abundances – found logarithmic slopes of -0.66 ± 0.05 and -0.44 for the combined radial profiles of iron and silicon, respectively, across their sample, compared to our slope of $-0.31^{+0.03}_{-0.05}$ for the mean metallicity (see Fig. 10). At a radius of r_{500}, Rasmussen & Ponman estimate an average iron abundance in groups to be ~ 0.1, whereas the extrapolation of the above best fit implies a mean metallicity of $Z \sim 0.15$ in clusters at the same radius.
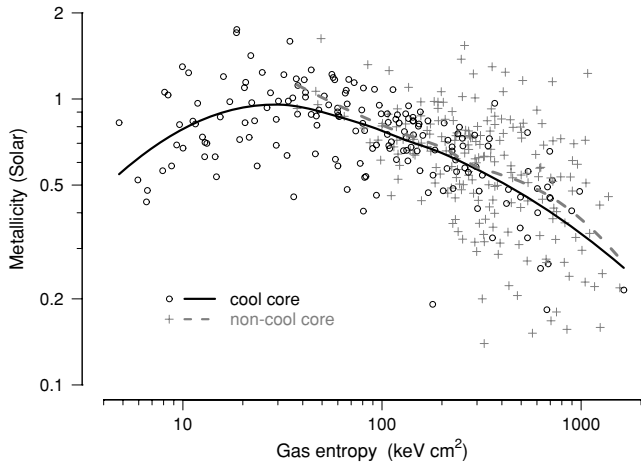
Figure 11. Projected gas metallicity versus entropy, with locally weighted fits to the CC and non-CC clusters plotted as solid and dashed lines, respectively.

The similar abundance patterns between CC and non-CC clusters can be seen by examining the gas metallicity as a function of entropy, plotted in Fig. 11. Also plotted are locally weighted curves for the combined points in each category, which demonstrate that there is very little difference between them, aside from the greater radial coverage in the centres of CC clusters. Since the gas entropy scales roughly linearly with radius (Fig. 3), the trend between metallicity and entropy mimics that seen in Fig. 9. However, a striking aspect of Fig. 11 is the almost complete absence of low-metallicity gas (i.e. <0.4–0.5 Solar) with low entropy ($S < 200$ keV cm^2). In general, it appears that the most enriched gas has low entropy, although the smoothed local regression suggests a turnover in this trend towards lower metallicity below ~ 30 keV cm^2. Interestingly, this entropy level corresponds to the threshold below which star formation appears to take place in the central galaxies of CC clusters (Rafferty, McNamara & Nulsen 2008; Voit et al. 2008). Thus, a reversal of the inverse trend between entropy and metallicity may reflect the loss of the most enriched gas from the hot phase in fuelling such star formation.

5 CLUSTER BIMODALITY AND THERMAL CONDUCTION

Clusters can be divided according to the presence or absence of a CC, and it is clear that the properties of these two categories differ substantially in terms of their temperature, density and entropy profiles. However, an important question to ask is, are these two types merely separate parts of the same continuous distribution, or do they really constitute distinct populations? If the latter holds true, then this would have interesting implications for models of self-similarity breaking via feedback and/or other non-gravitational processes.

To address this issue, we return to the power-law fits to the entropy profiles described in Section 4.2.1. The probability distribution of logarithmic slopes is plotted as a kernel density estimate in Fig. 12, with the positions of the raw values also indicated. It can be seen that two peaks are visible in the distribution, suggestive of bimodality in the cluster population. We performed a maximum likelihood fit to the unbinned entropy slope values with both a single and a pair of (equally weighted) Gaussians, using the FITDISTR function in the MASS package in R. The single Gaussian best-fitting mean value was
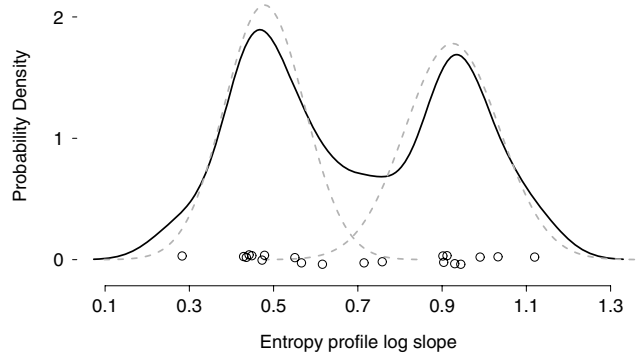
Figure 12. Kernel-smoothed (with a Gaussian of standard deviation 0.07) probability density plot of the best-fitting logarithmic slope of the entropy profile (solid line), showing the raw values as randomly 'jittered' points over the x-axis. The dashed curves are the components of the best-fitting bimodal Gaussian distribution to the data (see text for details). With the exception of Abell 2142, all the clusters above 0.7 are CC and all those below are non-CC.

$\mu = 0.70 \pm 0.05$ with standard deviation of $\sigma = 0.25 \pm 0.04$, and the best-fitting double-Gaussian values were

$$\mu 1 = 0.48 \pm 0.04 \quad \sigma 1 = 0.10 \pm 0.03$$
$$\mu 2 = 0.92 \pm 0.04 \quad \sigma 2 = 0.11 \pm 0.03.$$

The two separate Gaussians are plotted as dashed curves in Fig. 12 and align closely with the peaks in the smoothed density distribution; the crossover point between these two Gaussians is 0.69 and is plotted as the dashed horizontal line in Fig. 5.

In order to provide a quantitative assessment of the putative bimodality in the population, we calculated both the Akaike information criterion (AIC; Akaike 1974) and the Bayesian information criterion (BIC; Schwarz 1978). These are standard statistics used in model selection (e.g. see Liddle 2007, for a discussion of their relative merits), based on the negative log-likelihood penalized according to the number of free parameters, with the model having the lowest value always being preferred. The corresponding values obtained are AIC = 4.65 (−0.49) and BIC = 6.64 (3.49) for the single (double) Gaussian model, implying a change in BIC of 4.0 in favour of the two component fit. Differences in BIC of between 2 and 6 indicate positive evidence against the model with the greater BIC value, with values above 6 indicating strong evidence against the model with the greater BIC value (e.g. Mukherjee et al. 1998), demonstrating that a bimodal distribution is clearly favoured over a unimodal distribution. Given that the sample was statistically selected, this therefore implies that two distinct categories of cluster exist.

The two separate distributions of entropy profile logarithmic slopes match the CC classification (with the exception of Abell 2142; see Section 4.2.1), show similar dispersion ($\sigma \sim 0.1$) and are well separated (the means differ by ~ 4 standard deviations). The means of the distributions are also in good agreement with the results obtained by fitting equation (3) to the CC and non-CC clusters separately, as summarized in Table 3.

While a power-law fit describes the entropy profiles of CC clusters quite well, it can be seen from Fig. 7 that the non-CC profiles appear to flatten increasingly at small radii. This raises the possibility that estimating the gradient from a power-law fit (albeit robustly) could bias the results. Therefore, to check our conclusions regarding bimodality, we have also evaluated the entropy profile logarithmic

slope at $0.05r_{500}$ as estimated from a locally weighted fit to the data (in log–log space), using the LOESS task in R (cf. Fig. 7), with a heavier smoothing (using a value of the 'span' parameter of 2), to increase the stability of the gradient measurements. Repeating the above analysis leads to best-fitting bimodal populations given by

$$\mu 1' = 0.26 \pm 0.09 \quad \sigma 1' = 0.28 \pm 0.07$$
$$\mu 2' = 0.97 \pm 0.03 \quad \sigma 2' = 0.08 \pm 0.02.$$

The corresponding values obtained are AIC = 25.4 (18.4) and BIC = 27.4 (22.4) for the single (double) Gaussian model, implying a change in BIC of 5.0 in favour of the two component fit. It can be seen that the non-CC slope is indeed flatter at this smaller radius (although with much greater dispersion), but that the conclusion that the population is bimodal is verified.

5.1 Conduction and thermal balance

One of the most intriguing aspects of the ICM is its resistance to runaway radiative cooling. Although galaxy feedback is a plausible mechanism for maintaining (or nearly maintaining) thermal balance in the centres of CC clusters, it is less clear if it can similarly affect non-CC clusters, which none the less have also short cooling times in their inner regions (Paper I). This is because non-CC clusters show no sign of mass dropout necessary to fuel AGN outbursts or supernova winds. However, heat transport by thermal conduction is likely to play an important role in such cases and is also very effective at stabilizing cooling within CC regions, provided the gas density is not too high (e.g. Conroy & Ostriker 2008; Guo et al. 2008).

Circumstantial evidence for the effectiveness of thermal conduction in counteracting cooling can be seen in the temperature profiles of CC clusters. As pointed out by Voigt et al. (2002), CCs at the limit of stabilization by conduction would have temperature gradients of the form $T \propto r^{0.4}$ in the case of bremsstrahlung emission, flattening to $T \propto r^{0.3}$ for line-dominated emission, which concurs well with observations of CC clusters (Paper I) and groups (O'Sullivan et al., in preparation), respectively. Furthermore, recent work by Voit et al. (2008) and Rafferty et al. (2008) indicates that star formation in the cores of clusters, resulting from unchecked cooling, only occurs when the gas entropy drops below a certain level ($\lesssim 30$ keV cm^2) which matches the threshold below which gas becomes thermally unstable against conduction.

The critical scale for thermal conduction is given by the Field length, which must exceed the characteristic size of the system in order to allow thermal balance to be maintained by smoothing out temperature fluctuations (Field 1965). Following Donahue et al. (2005) and Voit et al. (2008), the Field length, λ_F, can be approximated as

$$\lambda_F = \left(\frac{\kappa T}{\rho_{\text{gas}}^2 \Lambda} \right)^{1/2} \approx 4 \text{ kpc} \left(\frac{S}{10 \text{ keV cm}^2} \right)^{3/2} f_c^{1/2}, \tag{4}$$

where κ is the *Spitzer* conduction coefficient with suppression factor f_c. This relation applies for the case of bremsstrahlung emission, where the cooling function varies with temperature, T, such that $\Lambda \propto T^{1/2}$, which renders λ_F a function of entropy only (Donahue et al. 2005).

In the limit of conductive thermal balance, where $r = \lambda_F$, equation (4) can be rearranged to yield an expression for the corresponding implied suppression factor:

$$f_c \approx 62.5 \frac{r^2}{S^3}, \tag{5}$$
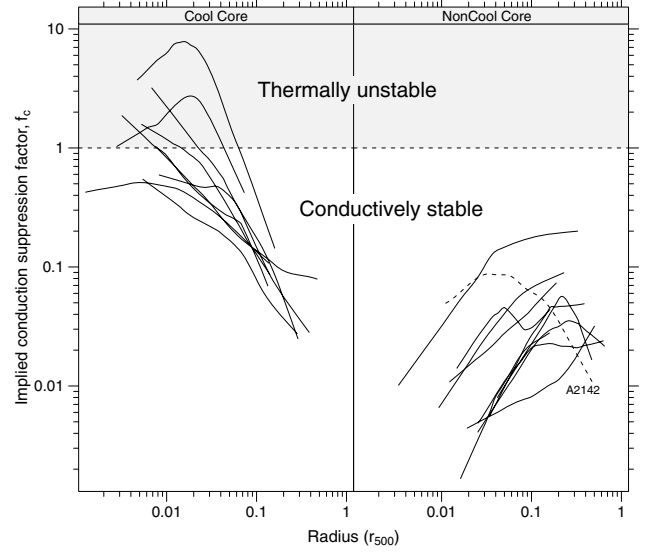
Figure 13. Implied *Spitzer* conductivity suppression factor as a function of scaled radius, grouped by CC type and plotted with identical axes. Each curve represents a locally weighted fit to the data points, to suppress small-scale fluctuations (see the text for details).

in terms of the radius, r (in kpc) and the entropy, S (in keV cm^2). The variation of this quantity with scaled radius is plotted for each cluster in Fig. 13, smoothed using the LOESS function in R and split by CC status. Also shown is the threshold of thermal stability, corresponding to conduction at the *Spitzer* rate, when $f_c = 1$. The striking aspect of Fig. 13 is the clear difference between the profiles of CC and non-CC clusters, in terms of both their shapes and locations on the plot: CC clusters having higher normalization and largely negative gradients compared to non-CC profiles, which all lie well within the conductively stable region with mostly positive gradients. Once again, the outlier cluster Abell 2142 (as seen in Fig. 5) stands out as an anomaly (the only non-CC curve aligned from bottom right to top left), which nevertheless retains similarities to both categories in that it lies within the range of the *non*-CC profiles while bearing closer resemblance to the CC profiles in shape.

The implication of Fig. 13 is that non-CC clusters are certainly capable of being stabilized by conduction alone, operating at no more than ∼10 per cent of the *Spitzer* rate and even much less effectively than that within their inner regions. By contrast, the CC clusters require values of $f_c \gtrsim 0.1$ within the peak temperature radius (∼0.15r_{500}; Paper I), rising sharply towards the centre and in some cases crossing into the region of thermal instability, corresponding to $f_c > 1$ (for NGC 5044, Abell 262, Abell 478, Abell 496 and 2A 0335+096). For these five clusters, an additional heat source would be required in order to maintain thermal balance. With the exception of A478, these are four of the five coolest CC clusters (see Table 2), which is unsurprising, since thermal conduction operates much less effectively at lower temperatures as the *Spitzer* conductivity, $\kappa \propto T^{5/2}$. Furthermore, all except Abell 496 show evidence of AGN-related disturbance in the form of X-ray cavities (Bîrzan et al. 2004) and both X-ray and radio disturbance in the case of NGC 5044 (David et al., in preparation). These results are in agreement with the findings of Voigt & Fabian (2004), who studied four of the same clusters: for Abell 2029 and Abell 1795 they also concluded that conductivity at or below the *Spitzer* level was able to

balance cooling everywhere inside the cooling radius, whereas this was not the case for Abell 478 and 2A 0335+096.

Theoretical considerations indicate that magnetohydrodynamic turbulence in the ICM could give rise to conduction suppression factors of ~0.2 (Narayan & Medvedev 2001), which is also consistent with results from the direct numerical simulations of Maron, Chandran & Blackman (2004), who favour $f_c \sim 0.1$–0.2. This would imply conductive stability for the non-CC clusters at all radii and for all CC clusters outside ~ 0.05–0.1r_{500} (Fig. 13). Taking all the f_c values for the non-CC clusters, we find the spread of values to be well fitted by lognormal distribution with a mean log (base 10) of -1.50 ± 0.03 and log standard deviation of 0.39 ± 0.02 corresponding to 0.032 with a 1σ range of 0.013–0.077.

Why, though, should a threshold for conduction stability give rise to a well-separated bimodal distribution of clusters, with a 'zone of avoidance' in between? Donahue et al. (2005) point out that clusters exceeding the threshold for conductive stability will continue to cool until some other form of heating intervenes, which would therefore lead to diverging populations. In which case, the fact that the non-CC f_c profiles are themselves not flat suggests that this threshold is spatially varying. Since the likely dominant cause of conduction suppression is magnetic fields, it follows that the configuration of magnetic field lines varies significantly with radius. Consequently, it is possible that the variation of f_c profiles amongst the non-CC clusters reflects the intrinsic variation in intracluster magnetic field configurations in the cluster population. In any case, the non-CC f_c profiles (except for A2142) all drop sharply inside ~0.1r_{500}, reaching values within the typical scale of the central cluster galaxy (~ 0.02r_{500}) consistent with the higher suppression factors of $\gtrsim$0.01 present in the interstellar medium of cluster galaxy coronae (Sun et al. 2007). This indicates that the transition within the ICM to higher suppression factors on galaxy scales may occur smoothly, suggesting a gradual variation in magnetic fields.

By contrast, the presence of cold fronts in the ICM implies sharply discontinuous magnetic fields, especially considering that such features occur at larger cluster radii, where f_c is greater. For example, in the case of Abell 2142, detailed analysis of the temperature gradient across the cold front indicates that conduction must be suppressed by at a factor of 250–2500 (Ettori & Fabian 2000), which is certainly far below the levels implied in Fig. 13, although these amount to globally averaged estimates. Such discontinuous configurations are possible in this case, since the magnetic field is likely to be stretched by tangental gas motions near the cold front, making it stronger and changing its structure compared to the rest of the ICM (Vikhlinin, Markevitch & Murray 2001).

A notable feature of Fig. 13 is the absence of any substantially flat profiles, in between the strongly negative gradients of the CC clusters and the mostly strongly positive (except for A2142) gradients of the non-CC clusters. A flat profile, lying along the conduction-stabilized threshold with a constant value of $f_c \leq 1$, would imply an entropy profile of the form $S \propto r^{2/3}$ (Donahue et al. 2005), which is close to the crossover point of 0.69 between the two distributions of entropy profile logarithmic slopes found in Section 5 (also plotted as the dashed horizontal line in Fig. 5). Thus, the divergence between CC and non-CC profiles seen in Fig. 13 mirrors the bimodality seen in the slopes of the entropy profiles described above.

6 DISCUSSION

The above results clearly indicate that bimodality is present in the cluster population, structured along the dichotomy between CC and non-CC clusters. Furthermore, the implication is that thermal

conduction alone is a plausible mechanism for stabilizing the ICM in non-CC clusters, whereas additional heating from galaxy feedback is necessary to achieve the same in CC clusters – a conclusion also reached by Guo et al. (2008). Conductive heat transfer could certainly explain why no significant temperature decline is observed in non-CC clusters, despite the short cooling times of gas in their cores (Paper I). However, by contributing to the heating of the cluster core, conduction also acts to reduce the amount of energy input required from additional sources such as AGN, in order to maintain thermal stability. This may therefore account for the observed lack of evidence for *strong* AGN heating in clusters (McNamara & Nulsen 2007).

Nevertheless, while feedback heating may not be necessary to stabilize non-CC clusters, it is clear from the results of the entropy-temperature scaling analysis in Section 4.2.2 that both CC and non-CC clusters show significant departures from self-similarity. Such similarity breaking is the unmistakable signature of non-gravitational physics, which suggests that the non-CC clusters must *also* have been impacted significantly by feedback (if not also radiative cooling) in their lifetimes. This possibility is consistent with the theoretical model of McCarthy et al. (2008), where non-CC clusters are formed from material that has experienced higher levels of preheating. In this picture, the influence of conduction could help to segregate the cluster population and stave off the formation of CCs in the most strongly preheated systems.

A related aspect is the role of mergers in cluster evolution, particularly given the close association between signatures of recent disruption, such as radio haloes, and the absence of a CC (e.g. Million & Allen 2008). Although suggesting a key role for thermal conduction in sustaining non-CC clusters, our results nevertheless certainly do not rule out merging as an alternative explanation for their existence. While recent simulations have concluded that cluster mergers cannot permanently erase CCs (Poole et al. 2006), it is possible that the additional influence of conduction could achieve this outcome and thereby provide an alternative path to a non-CC state. In this situation, the temporary fragmentation of a CC that can take place in a merger (Poole et al. 2008) could plausibly lead to conductive dissipation of the resulting blobs of cool gas, whose size can easily fall below the Field length, provided the magnetic field configuration is favourable. Since conduction lowers the threshold necessary to transition from a state where additional feedback is required (i.e. in a CC), to one where conduction alone can maintain stability (i.e. a non-CC), the transformation from CC to non-CC status is correspondingly more achievable.

However, notwithstanding this appealing explanation of bimodal populations, it is also clear that the key role that conduction can play in stabilizing *clusters* against cooling instabilities cannot easily extend to galaxy groups, where the lower gas temperatures render it much less effective (the conduction coefficient, $\kappa \propto T^{5/2}$). Therefore, the impact of merging activity may be more short-lived in galaxy groups, without the contribution of significant conductive heat transfer to impede re-formation of a CC. This suggests that non-CC groups are likely to have been *recently* disrupted; by contrast, conduction in clusters could sustain a non-CC state in post-mergers long after disruption. Nevertheless, it remains to be seen whether a consistent thermodynamic picture of ICM evolution in both groups *and* clusters can be developed.

The similarity of the ICM metallicity in CC and non-CC clusters is noteworthy as the only property of the gas that does not differ significantly between the two types, at least within the region of overlap seen in this sample. This fact alone provides evidence that strong mixing of gas cannot preferentially have affected non-CC

clusters – as a result of merging activity, for example. However, the width of the metallicity peak in the cluster cores appears significantly ($\gtrsim 2\times$) broader than the stellar distribution of the brightest cluster galaxy, as previously noted by Rebusco et al. (2005), which implies some mechanism to transport metals into the ICM. Rebusco et al. speculate that this might be caused by AGN-driven gas motion, as also favoured by the recent theoretical modelling of Rasera et al. (2008). However, if AGN are responsible for diffusing the enriched gas, then the similarity of cluster metallicity profiles implies an equally prominent role for AGN outflows in non-CC clusters, despite the lack of evidence for significant AGN disruption in such cases.

7 CONCLUSIONS

Using the statistically selected sample of 20 galaxy clusters presented in Paper I, we have studied the density, entropy and metallicity of the ICM as a function of radius, focussing on the comparison between clusters with CCs and those without. We describe an improved method of estimating the cluster mean temperature and fiducial scaling radius r_{500}, which we use to explore systematic trends in cluster gas properties across the sample.

We find that the gas density is systematically higher in the cores of CC clusters, and that the ICM is progressively depleted in less massive systems. We also find a clear departure from self-similar scaling in the gas entropy which is consistent with the modified scaling of $S \propto \overline{T}^b$ with $b = 0.65$ from Ponman et al. (2003): at $0.1r_{500}$ the best-fitting scaling is $b = 0.66 \pm 0.10$ and 0.71 ± 0.21 for CC and non-CC clusters, respectively. However, the dependency on temperature strengthens when all the clusters are combined, to a nearly self-similar value of $b = 0.92 \pm 0.12$, and similar results are obtained in all three cases for entropy measured at $0.15r_{500}$ versus mean temperature. This demonstrates that similarity breaking (i.e. $S \propto T^{\sim 2/3}$) can exist in the separate populations of CC and non-CC clusters, even while the combined population shows consistency with self-similarity.

The metallicity of the gas shows no evidence of a systematic variation with $\overline{T}$, but declines with radius such that $Z \propto r^{-0.31\pm0.04}$ outside $0.014r_{500}$ (comparable to the size of any central dominant galaxy), for both CC and non-CC clusters alike. Inside this point, there is substantial divergence in the metallicity, with a few CC clusters showing sharply decreasing Z towards the centre while others possess continually rising profiles. At large radii, there is no indication of any flattening in the metallicity profile to at least $\sim 0.5r_{500}$, where the *Chandra* field of view limits the data. We study gas metallicity as a function of entropy and find a striking lack of low-metallicity gas (i.e. <0.4–0.5 Solar) with low entropy ($S <$ 200 keV cm^2). Above ~ 100 keV cm^2, the metallicity declines with increasing entropy in an identical fashion for both CC and non-CC clusters.

We address the issue of bimodality in cluster properties by studying the distribution of logarithmic slopes obtained from power-law fits to individual cluster entropy profiles (i.e. $S \propto r^a$). We find that a double-Gaussian distribution is strongly preferred over a unimodal Gaussian distribution, using maximum likelihood fits to the unbinned values, employing both the BIC and AIC model selection tests. The best-fitting means of the two distributions are $a = 0.92 \pm 0.04$ and 0.48 ± 0.04, with a standard deviations of 0.1 in both cases. Given the statistically selected nature of the sample, this demonstrates that two distinct categories of cluster exist, which have important implications for models of galaxy feedback and cluster similarity breaking.

We explore the impact of thermal conduction on the ICM by studying the implied conduction suppression factor, f_c, as a function of radius. We find that the profiles of f_c differ sharply between CC and non-CC clusters consistent with two distinct populations. We conclude that conduction alone is capable of stabilizing non-CC clusters against catastrophic cooling, while in CC clusters some feedback is required in addition to conduction to maintain thermal balance, in agreement with the findings of Guo et al. (2008). Taking all the f_c values for the non-CC clusters, we find the spread of values to be well fitted by lognormal distribution with a mean log (base 10) of -1.50 ± 0.03 and log standard deviation of 0.39 ± 0.02 corresponding to 0.032 with a 1σ range of 0.013–0.077.

REFERENCES

Akaike H., 1974, IEEE Trans. Autom. Control, 19, 716
Akritas M. G., Bershady M. A., 1996, ApJ, 470, 706
Baldi A., Ettori S., Mazzotta P., Tozzi P., Borgani S., 2007, ApJ, 666, 835
Balogh M. L., Pearce F. R., Bower R. G., Kay S. T., 2001, MNRAS, 326, 1228
Bauer F. E., Fabian A. C., Sanders J. S., Allen S. W., Johnstone R. M., 2005, MNRAS, 359, 1481
Bîrzan L., Rafferty D. A., McNamara B. R., Wise M. W., Nulsen P. E. J., 2004, ApJ, 607, 800
Blanton E. L., Sarazin C. L., McNamara B. R., Clarke T. E., 2004, ApJ, 612, 817
Bower R. G., 1997, MNRAS, 288, 355
Cole S., 1991, ApJ, 367, 45
Conroy C., Ostriker J. P., 2008, ApJ, 681, 151
Croston J. H. et al., 2008, A&A, 487, 431
De Grandi S., Molendi S., 2001, ApJ, 551, 153
De Grandi S., Ettori S., Longhetti M., Molendi S., 2004, A&A, 419, 7
Donahue M., Voit G. M., O'Dea C. P., Baum S. A., Sparks W. B., 2005, ApJ, 630, L13
Donahue M., Horner D. J., Cavagnolo K. W., Voit G. M., 2006, ApJ, 643, 730
Ettori S., Brighenti F., 2008, MNRAS, 387, 631
Ettori S., Fabian A. C., 2000, MNRAS, 317, L57
Fabian A. C., 1994, ARA&A, 32, 277
Field G. B., 1965, ApJ, 142, 531
Finoguenov A., Reiprich T. H., Böhringer H., 2001, A&A, 368, 749
Fukugita M., Hogan C. J., Peebles P. J. E., 1998, ApJ, 503, 518
Gonzalez A. H., Zaritsky D., Zabludoff A. I., 2007, ApJ, 666, 147
Grevesse N., Sauval A. J., 1998, Space Sci. Rev., 85, 161
Guo F., Oh S. P., Ruszkowski M., 2008, ApJ, 688, 859
Ikebe Y., Reiprich T. H., Böhringer H., Tanaka Y., Kitayama T., 2002, A&A, 383, 773
Katz N., 1992, ApJ, 391, 502
Katz N., White S. D. M., 1993, ApJ, 412, 455
Kay S. T., da Silva A. C., Aghanim N., Blanchard A., Liddle A. R., Puget J.-L., Sadat R., Thomas P. A., 2007, MNRAS, 377, 317
Koenker R. W., 2005, Quantile Regression. Cambridge Univ. Press, Cambridge
Liddle A. R., 2007, MNRAS, 377, L74

Lloyd-Davies E. J., Ponman T. J., Canon D. B., 2000, MNRAS, 315, 689

Markevitch M. et al., 2000, ApJ, 541, 542

Maron J., Chandran B. D., Blackman E., 2004, Phys. Rev. Lett., 92, 045001

McCarthy I. G., Babul A., Bower R. G., Balogh M. L., 2008, MNRAS, 386, 1309

McNamara B. R., Nulsen P. E. J., 2007, ARA&A, 45, 117

Million E. T., Allen S. W., 2008, MNRAS, submitted (arXiv:0811.0834)

Mukherjee S., Feigelson E. D., Jogesh Babu G., Murtagh F., Fraley C., Raftery A., 1998, ApJ, 508, 314

Narayan R., Medvedev M. V., 2001, ApJ, 562, L129

Peterson J. R., Fabian A. C., 2006, Phys. Rep., 427, 1

Peterson J. R. et al., 2001, A&A, 365, L104

Piffaretti R., Jetzer P., Kaastra J. S., Tamura T., 2005, A&A, 433, 101

Ponman T. J., Cannon D. B., Navarro J. F., 1999, Nat, 397, 135

Ponman T. J., Sanderson A. J. R., Finoguenov A., 2003, MNRAS, 343, 331

Poole G. B., Fardal M. A., Babul A., McCarthy I. G., Quinn T., Wadsley J., 2006, MNRAS, 373, 881

Poole G. B., Babul A., McCarthy I. G., Sanderson A. J. R., Fardal M. A., 2008, MNRAS, 391, 1163

Pratt G. W., Arnaud M., Pointecouteau E., 2006, A&A, 446, 429

Pratt G. W., Böhringer H., Croston J. H., Arnaud M., Borgani S., Finoguenov A., Temple R. F., 2007, A&A, 461, 71

R Development Core Team, 2008, R: A Language and Environment for Statistical Computing. R Foundation for Statistical Computing, Vienna, Austria

Rafferty D. A., McNamara B. R., Nulsen P. E. J., 2008, ApJ, 687, 899

Rasera Y., Lynch B., Srivastava K., Chandran B., 2008, ApJ, 689, 825

Rasmussen J., Ponman T. J., 2007, MNRAS, 380, 1554

Rebusco P., Churazov E., Böhringer H., Forman W., 2005, MNRAS, 359, 1041

Reiprich T. H., Böhringer H., 2002, ApJ, 567, 716

Sanderson A. J. R., Ponman T. J., 2003, MNRAS, 345, 1241

Sanderson A. J. R., Ponman T. J., O'Sullivan E., 2006, MNRAS, 372, 1496 (Paper I)

Schwarz G., 1978, Ann. Stat., 6, 461

Strickland D. K., Stevens I. R., 2000, MNRAS, 314, 511

Suginohara T., Ostriker J. P., 1998, ApJ, 507, 16

Sun M., Jones C., Forman W., Vikhlinin A., Donahue M., Voit M., 2007, ApJ, 657, 197

Sun M., Voit G. M., Donahue M., Jones C., Forman W., 2008, ApJ, in press (arXiv:0805.2320)

Tozzi P., Norman C., 2001, ApJ, 546, 63

Vikhlinin A., Markevitch M., Murray S. S., 2001, ApJ, 549, L47

Vikhlinin A., Markevitch M., Murray S. S., Jones C., Forman W., Van Speybroeck L., 2005, ApJ, 628, 655

Vikhlinin A., Kravtsov A., Forman W., Jones C., Markevitch M., Murray S. S., Van Speybroeck L., 2006, ApJ, 640, 691

Voigt L. M., Fabian A. C., 2004, MNRAS, 347, 1130

Voigt L. M., Schmidt R. W., Fabian A. C., Allen S. W., Johnstone R. M., 2002, MNRAS, 335, L7

Voit G. M., Bryan G. L., Balogh M. L., Bower R. G., 2002, ApJ, 576, 601

Voit G. M., Cavagnolo K. W., Donahue M., Rafferty D. A., McNamara B. R., Nulsen P. E. J., 2008, ApJ, 681, L5

Zhang Y.-Y., Böhringer H., Finoguenov A., Ikebe Y., Matsushita K., Schuecker P., Guzzo L., Collins C. A., 2006, A&A, 456, 55

This paper has been typeset from a TeX/LaTeX file prepared by the author.